Time Encoded Communications for Human Area Network Biomonitoring

Csaba Káldy, Aurel A. Lazar, *Fellow, IEEE*, Ernő K. Simonyi, and László T. Tóth

Abstract—**Power constraints play a key role in designing Human Area Networks (HANs) for biomonitoring. To alleviate the power constraints, we advocate a design that uses an asynchronous time encoding mechanisms for representing biomonitoring information and the skin surface as the communication channel. Time encoding does not require a clock while allows perfect signal recovery; the communication channel is operated below 1 MHz. We (i) review the fundamental theory behind time encoding and signal recovery, (ii) describe the implementation of a HAN prototype and (iii) present research data obtained from our experimental platform. We demonstrate that the fidelity of the proposed signal representation and transmission scheme is well above the biomedical monitoring requirements even in the case of additive channel-noise and neighboring channel interference. Consequently, the traditional HAN architecture consisting of clocked A/D converters feeding into digital RF channels can be replaced with a less power demanding time encoding/decoding pair that uses the skin surface as a communications channel.**

I. INTRODUCTION

Energy efficiency is of extreme importance in certain biomedical or health-monitoring applications such as pulseoximetry, electrocardiography (ECG), and electroencephalography (EEG). In contrast, the requirements for accuracy and speed (bandwidth) are rather modest. For example, 8-bit accuracy and 100-500 Hz bandwidth is typical in ECG and EEG systems [2]. The energy consumption of the body-mounted sensors is the most critical factor. More power can be assigned to the personal digital assistant (PDA) placed close to or on the human body. The sensor signals are often evaluated at a remote site (center) where practically unlimited power can be assumed.

Technological evolution of low-power integrated circuits (ICs), and wireless communication allows the production of low-cost, miniature, lightweight, intelligent physiological sensors. These units enable the deployment of sensor networks for health monitoring often referred to as human, personal or body area networks. In these solutions analog-to-digital (A/D) conversion and wireless digital transmission is carried out by the sensor nodes using radio-frequency (RF) channels via tiny antennas. Power dissipation due to both A/D conversion and digital transmission are two major limitations. Ongoing development can be observed in the literature for low-power

A/D converters, see, e.g., [18] and the references therein. In typical recent RF applications the amount of energy needed for transmitting one single bit amounts to that of executing about 1000 of 32-bit computations [7]. Intelligent on-sensor signal processing methods have been investigated with the potential to save power (hence extend battery life) by transmitting processed data rather than raw signals [6].

Fig. 1 depicts an alternative method for biomonitoring that is closely related to a method originally proposed for digital transmission in personal area network (PAN) applications [22], [23], [19]. As shown, several sensors (only 3 sensors are shown) and the PDA are connected to the human body via insulators. The transmit power can be reduced by using the skin surface as a short range communication channel. Briefly, since any two distinct points of the human body are interconnected
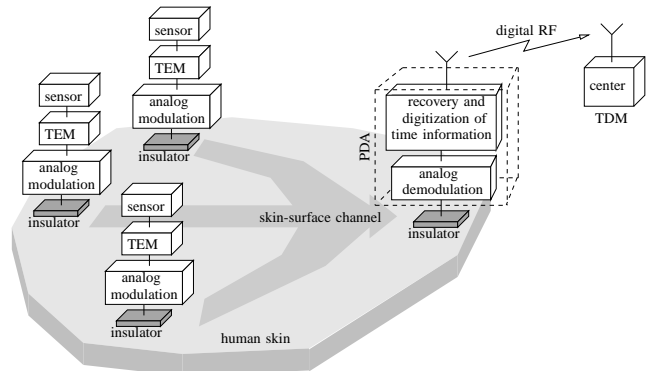

Fig. 1. The basic architecture of the Human Area Network for biomonitoring.

via capacitive coupling, signals with high enough frequency content can travel between any two points. Whereas a radio transmitting PAN device needs to be operated at frequencies in the MHz-to-GHz range in order to efficiently transmit biomonitoring information, electrostatic coupling reaches the same efficiency by running the devices at much lower frequencies (0.1 to 1 MHz). Given that the energy consumption of electronic devices increases with frequency, substantial amount of energy can be saved [22]. Note that, data transmitted through the human body eventually escapes through the feet into the ground, thereby minimizing the chance of intercept and, thus, providing secure communications [19].

Instead of using A/D converters that represent biomonitoring information in the amplitude domain, we propose to represent the same information in the time domain with Time Encoding Machines (TEMs) [11]. TEMs can be typically implemented as low-power, nonlinear, asynchronous, analog circuits and are suitable for IC implementation [20], [9]. At

a remote site signal reconstruction and application-specific evaluations are carried out. The reconstruction algorithm and its implementation in software and/or hardware is referred to as the Time Decoding Machine (TDM) [11].

TEMs represent analog signals in the time domain without any loss of information [11]. Since such circuits do not use a clock, they are candidates for replacing the traditional A/D converters based on clocked sigma/delta modulators or other low power converters [18]. In a HAN environment for biomonitoring a number of problems arise including crosstalk from neighboring sensors and additive noise.

The goal of this paper is to demonstrate that using of the shelf components, the traditional A/D converter can be replaced by a TEM/TDM pair and the resulting system (shown in Fig. 1) displays an accuracy that is well above typical biomonitoring requirements. This provides a basis for using low power TEMs for representing biomonitoring information in HANs.

This paper is organized as follows. In section II we present the overall architecture of the HAN and summarize the basic principles of time encoding and decoding. We also review a class of parameter insensitive stable algorithms for signal recovery. Implementation details of the HAN prototype are described in Section III. Finally, performance evaluation of the HAN prototype is given in Section IV.

II. THE ARCHITECTURE OF THE HAN EXPERIMENTAL PLATFORM

A. The Architecture of the Human Area Network

Fig. 1 shows the proposed HAN architecture in block diagram form. As seen, each sensor drives a TEM whose output undergoes analog modulation for increased frequency content. The modulators are connected to the human body via an insulator. After strong attenuation and often corruption by noise and/or low-frequency interference, the aggregate of the modulated signals becomes available at another location of the human body via another insulator. The received signal is first demodulated after the appropriate sensor is selected. Based on the demodulator output, the PDA determines the time information contained in the demodulated (selected) signal, quantizes the latter, and forwards it in digital form to the remote center for reconstruction.

The skin-surface channel has been shown to have substantially less power requirements compared to RF channels [22], [23], [19]. The reduced power requirements of (asynchronous) TEMs when compared to (clocked) A/D converters have also been been extensively documented in the literature [3], [16]. Whether the TEM/TDM pair can be employed in the architecture above with a skin-channel that has strong and unpredictable attenuation in a practical low power application has received, however, little attention.

B. TEM and TDM Building Blocks

The TEM that we built (see [11] and the references therein), is the asynchronous sigma/delta modulator (ASDM) [8], [17] consisting of an integrator and a symmetrically-centered Schmitt trigger. Other TEM realizations include integrate-and-fire neurons [12] and frequency modulators [11]. More general TEMs are described in [14].
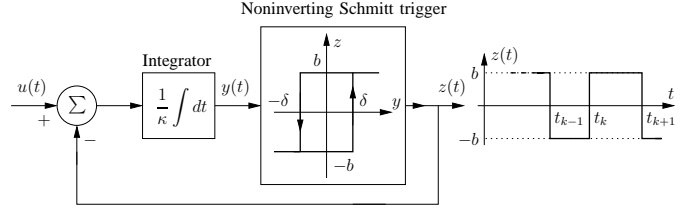

Fig. 2. TEM realized as an asynchronous sigma/delta modulator.

The schematic diagram of the TEM employed is shown in Fig. 2. $u(t)$ is a signal bandlimited to $[-\Omega, \Omega]$; κ, δ and b are circuit parameters, c is the amplitude bound and $|u(t)| \leq c < b$. Since the TEM output $z(t)$ takes either the values b or $-b$, the input to the integrator is either $u(t) + b$ or $u(t) - b$. Finally, since $|u(t)| < b$, the integrator output $y(t)$ is a strictly increasing or decreasing function for $t \in [t_k, t_{k+1}]$ and thus either $y(t_k) = \delta$ or $y(t_k) = -\delta$.

The TEM circuit in Fig. 2 is described by the t-transform [11]

$$\int_{t_k}^{t_{k+1}} u(t)dt = q_k, \tag{1}$$

where $q_k = b(-1)^k(2\kappa\delta - T_k)$ with $T_k = t_{k+1} - t_k$ for all $k, k \in \mathbb{Z}$ ($\mathbb{Z}$ denotes the integers). It is easy to see that the T_k's are bounded by:

$$\frac{2\kappa\delta}{b+c} \leq T_k \leq \frac{2\kappa\delta}{b-c}. \tag{2}$$

Therefore, the integrals of $u(t)$ over fixed time intervals are available at the decoder as a linear function of a bounded time sequence.

The mathematical approach for devising the TDM algorithm is closely related to the one used in irregular sampling and is built on frame theory, see, e.g., [4] or [1]. Related techniques are also needed to establish Nyquist-type rate conditions under which $u(t)$ can be perfectly reconstructed in terms of the integrals in (1), hence the T_k's [11], [12].

Theorem 1 *If the Nyquist-type rate condition*

$$\kappa\delta < \frac{b-c}{2} \cdot \frac{\pi}{\Omega} \tag{3}$$

is satisfied, the bandlimited input signal $u = (u(t)), t \in \mathbb{R}$, can be recovered as

$$u(t) = \sum_{\ell \in \mathbb{Z}} c_\ell g(t - s_\ell), \tag{4}$$

where $s_\ell = (t_\ell + t_{\ell+1})/2$ and

$$g(t) = \frac{\sin(\Omega t)}{\pi t} \tag{5}$$

is the impulse response of an ideal lowpass filter (LPF) with cutoff frequency Ω. The set of coefficients (c_ℓ), $\ell \in \mathbb{Z}$, satisfy

the system of linear equations

$$\sum_{\ell \in \mathbb{Z}} \underbrace{c_\ell}_{[\mathbf{c}]_\ell} \underbrace{\int_{t_k}^{t_{k+1}} g(s - s_\ell)ds}_{[\mathbf{G}]_{k\ell}} = \underbrace{q_k}_{[\mathbf{q}]_k}, \quad (6)$$

for all $k, k \in \mathbb{Z}$. Finally, the matrix $\mathbf{G}$, and the vectors $\mathbf{q}$ and $\mathbf{c}$ introduced above, verify the linear equation

$$\mathbf{Gc} = \mathbf{q}. \quad (7)$$

Since $\mathbf{G}$, $\mathbf{q}$ and $\mathbf{c}$ are infinite dimensional, the mathematical formalism above cannot be directly implemented. In practice only a finite set of the T_k's is available for signal reconstruction.

An efficient real-time TDM can be developed, however, using an overcomplete stitching formulation of signal recovery [13]. This involves two steps. First, we shall consider the covering sequence $[t_i, t_{i+N}], i \in \mathbb{Z}$, of the real line $\mathbb{R}$, where N is an arbitrary positive integer and approximate $u(t)$ on $[t_i, t_{i+N}]$ by the periodic bandlimited signal

$$u_i(t) = \sum_{n=0}^{N} j\left(\Omega - n\frac{2\Omega}{N}\right)d_{i,n}e^{j(-\Omega+n\frac{2\Omega}{N})t}. \quad (8)$$

The bandwidth and the period of $u_i(t)$ are Ω and $2N\pi/\Omega$ (for $N \geq 1$), respectively. Here $d_{i,n}$ is a set of coefficients whose values are to be determined as follows.

Proposition 1 *The coefficients $[\mathbf{d}_i]_n = d_{i,n}$ satisfy the matrix equation*

$$\mathbf{V}_i\mathbf{d}_i = \mathbf{D}_i\mathbf{P}\mathbf{q}_i, \quad (9)$$

for all $i, i \in \mathbb{Z}$, where $[\mathbf{V}_i]_{nm} = e^{jm2\Omega t_{i+n}/N}$ is a Vandermonde matrix, $\mathbf{D}_i = diag(e^{j\Omega t_{i+n}})$ is a diagonal matrix, $\mathbf{P}$ is an upper triangular matrix with values $[\mathbf{P}]_{nm} = 1$ and $[\mathbf{P}]_{nm} = 0$ for $n < m+1$ and $n \geq m+1$, respectively, and $[\mathbf{q}_i]_n = q_{i+n}$, for all $n, m = 0, \ldots, N$.

Second, by stitching the finite dimensional coverings together a natural approximation of the bandlimited signal $u = u(t), t \in \mathbb{R}$, is given by

$$\hat{u}(t) = \sum_{n \in \mathbb{Z}} w_n(t)u_{nJ}(t), \quad (10)$$

where $w_n(t)$ is a window function and J is a design parameter [13]. Due to the representation above, the window introduces a spreading of the bandwidth to $\Omega + \nu$, where ν is also a design parameter. Sampling the recovered signal at time instances kS with $S < \pi/(\Omega + \nu)$ for all $k, k \in \mathbb{Z}$, largely avoids aliasing [13].

Algorithm 1 *The reconstructed signal in discrete time (DT) is given by $\hat{u}(kS) * h[k]$, where the $h[k]$ is the impulse response of a DT LPF with (digital) cutoff frequency $\pi/(1+\nu/\Omega)$ and $*$ denotes the convolution.*

The algorithm above requires the exact knowledge of the key parameters κ and δ of the TEM. As was previously noted

in [11], by adding equation (1) for k and $k+1$, respectively, we obtain the relationship

$$q_{k+1} + q_k = \int_{t_k}^{t_{k+2}} u(t)dt = b(-1)^k(T_{k+1} - T_k). \quad (11)$$

The latter is a description of the TEM that is *insensitive* with respect to the circuit parameters κ and δ. The Schmitt-trigger height b merely appears as a generally tolerable scaling factor. This observation is the basis for an insensitive algorithm for determining the coefficients in (8). The corresponding algorithm developed in [13] is included in Appendix VI-A.

As shown in [13], the recovery algorithm is (i) insensitive with respect to the TEM circuit parameters, (ii) suitable for a real-time TDM implementation, and (iii) avoids numerical overflow. Further details and pointers can be found in [13].

III. IMPLEMENTATION OF THE HAN PROTOTYPE

A. Experimental Environment

Our *controlled* environment for measurements and evaluations is depicted in Fig. 3. Exact error evaluations require the accurate knowledge of the input signals. Since real sensors do not faithfully represent their input, we opted to employ ECG recorded signals instead. As seen, the definition of the input signal $u(t)$, the implementation of the PDA and the TDM, and the performance evaluation were carried out in a computational environment.
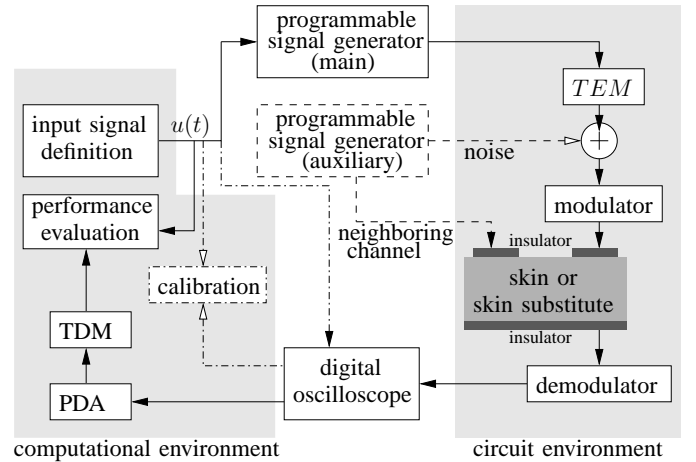

Fig. 3.   Measurement and evaluation setup corresponding to Fig. 1.

The TEM, the modulator, and the demodulator were implemented using standard discrete-component circuit elements and commercially available ICs. In our experiments we used both skin and a skin substitute (a wet sponge placed in a metalized plastic bag used for electrostatic discharge storage [19]).

The main (solid line) and the auxiliary (dashed line) programmable generators (Tektronix AFG 3252) create $u(t)$ shown in Fig. 4(b) and the interfering signals (crosstalk from other channel and noise), respectively. Any node voltage in the circuits can be measured and the measurements (samples with given sampling frequency) can be stored by a digital oscilloscope (Tektronix DPO 7104). A companion

software package (ArbExpress, Tektronix) allows data transfer between the computational environment and the generator and/or oscilloscope using the CSV (comma-separated value) file format. As shown, the samples of the demodulator output serve as input to the reconstruction (PDA and TDM) and the performance evaluation module. The calibration unit evaluates relevant error measures and establishes the accuracy limits of the arrangement. For completeness, we included a brief description of error measures and calibration in Appendix VI-B.

B. Reconstruction Accuracy in the Computational Environment

In order to emulate a realistic class of sensor-generated signals, we selected an ECG signal from the MIT-BIH public arrhythmia database [15]. This database contains a number of ambulatory ECG recordings digitized at 360 samples per second with 11-bit resolution over a 10 mV range.
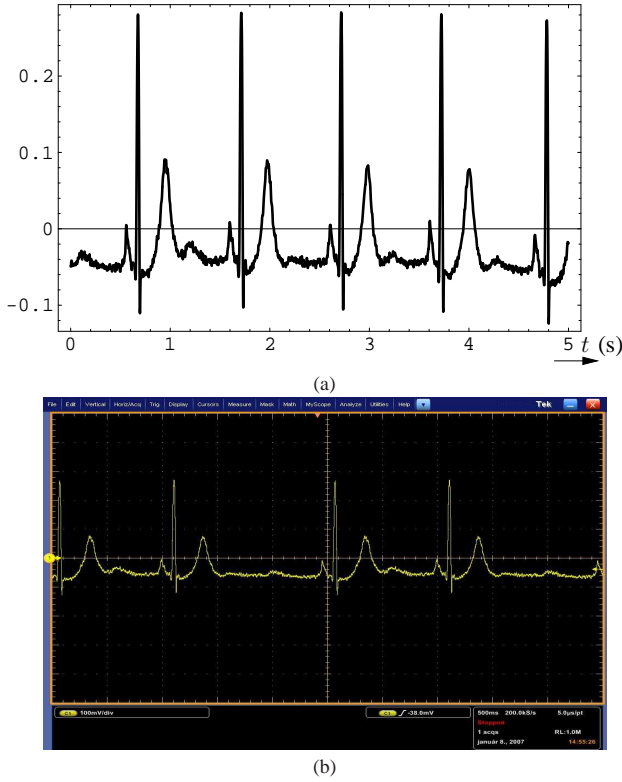

(a)

(b)

Fig. 4. ECG signal segment after a 7-th order polynomial interpolation (a) and measured result of the periodic input generated by a Fourier-series expansion with 750 Fourier-coefficients (b).

One of the (scaled) signal segments obtained after a 7-th order polynomial interpolation is shown in Fig. 4(a). Due to measurement constraints (see also Section VI-B in the Appendix), we employed a periodic input in our experimental platform. A periodic bandlimited waveform $u(t)$ was generated by expanding a segment of length 2.5 s of the signal in Fig. 4(a) into Fourier-series. The fast FFT algorithm computed 750 Fourier coefficients. Measured results of $u(t)$ so obtained and employed in the subsequent experiments are shown in Fig. 4(b). Therefore the bandwidth of $u(t)$ amounts to $\Omega =$
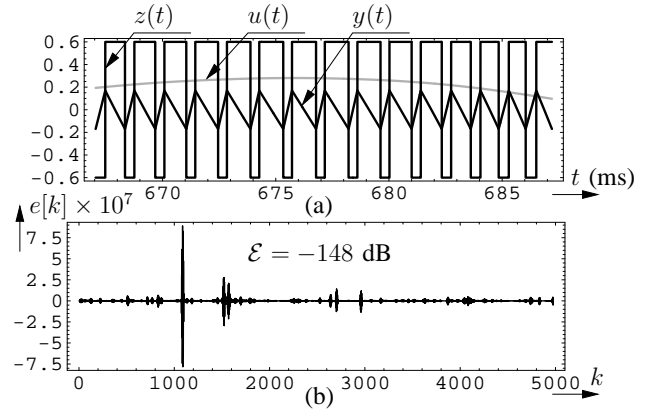

Fig. 5. TEM signals of Fig. 2 in a reduced range (a) and the overall reconstruction error defined in (A-4) (b).

$750 \times (2\pi/2.5) = 2\pi \times 300$ rad/s. As shown, $c = 0.3$ is an appropriate amplitude bound on the emulated ECG signal.

With TEM parameters $\delta = 0.17$, $b = 0.6$, and $\kappa = 0.001$ s, the condition in (3) is satisfied with $\kappa\delta = 0.402(b-c)\pi/\Omega$. For $u(t)$ in Fig. 4(b) the numerical calculation of 4975 T_k's was carried out by solving (1) recursively. Using these values we determined the TEM signals $y(t)$ and $z(t)$ for visualization purposes as shown in Fig. 5(a). Setting the sampling rate of the TDM to $S = \pi/(4\Omega) = 3.472$ ms, the recovery error evaluated according to (A-4) is shown in Fig. 5(b). Thus, under *ideal* circumstances (TEM/TDM pair only) the accuracy of signal recovery satisfies most requirements in practice.

C. The TEM Circuit

Fig. 6 shows the circuit implementation of the TEM in Fig. 2 using resistors and capacitors with 2% tolerance, LF256 opamps, and diodes. The middle opamp with the 47 nF capacitor and 28 kΩ resistor implements the integrator. The rightmost opamp with resistors 1 kΩ, 56.3 kΩ, 11.5 kΩ, and the diodes realizes the Schmitt trigger. The diodes force the Schmitt-
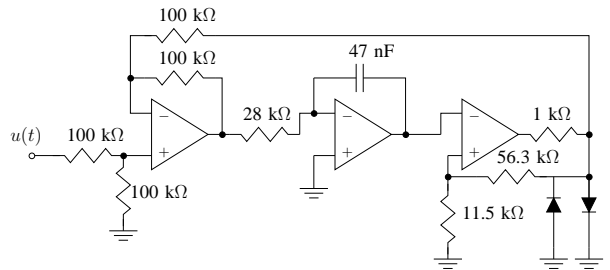

Fig. 6. Circuit implementation of the time encoding machine.

trigger output to take voltages around ± 0.6 V independent of the ± 9 V power supply voltages of the opamps (not shown). In this way, the TEM can be operated properly by batteries for relatively long time. The adder implemented by the leftmost opamp and the 100 kΩ resistors allow measuring the sum of $u(t)$ and the Schmitt-trigger output for test purposes. With the resistance and capacitance values shown, we set the same TEM parameter values (b, δ, and κ) as those in the example of Section III-B. With zero input, the self-oscillation frequency
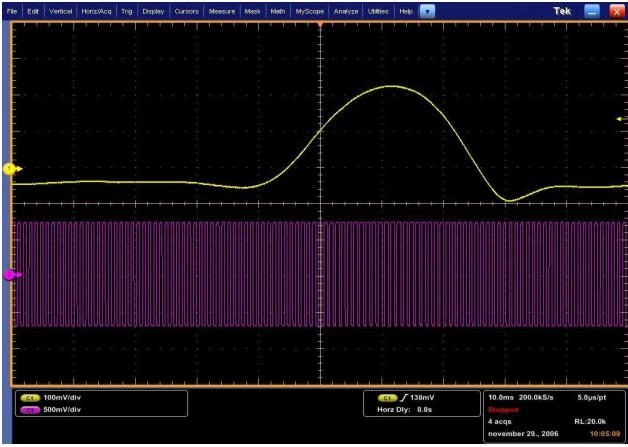
Fig. 7. Small input segment of Fig. 4(b) (upper trace) and the corresponding TEM output (lower trace). The scope's sampling frequency is 200 kHz.

of the TEM output turned out to be around 900 Hz. This measurement is close to the duty cycle value of 882.35 Hz of the ASDM obtained by setting $c = 0$ [11], [17]. The upper and lower trace of Fig. 7 show measured results of a small input segment of Fig. 4(b) and the corresponding TEM output, respectively.

D. The Recovery of the T_k's

The schematic of modulation and demodulation is depicted in Fig. 8. First, $s(t)$ is created by pulse shaping $z(t)$ (see [10] for a discussion on pulse shaping). As a result, the bandwidth of $s(t)$ is about 30 kHz. $m(t)$ is obtained by AM-modulating $s(t)$ with a rectangular carrier with frequency of $f_M = 354$ kHz. $d(t)$ is the AM demodulator output of a sensitive receiver of 30 kHz bandwidth. The receiver was built with a CSF455 type ceramic filter and the TDA 1046 chip. We employed a highly sensitive receiver because the skin-surface channel has a strong and unpredictable attenuation.
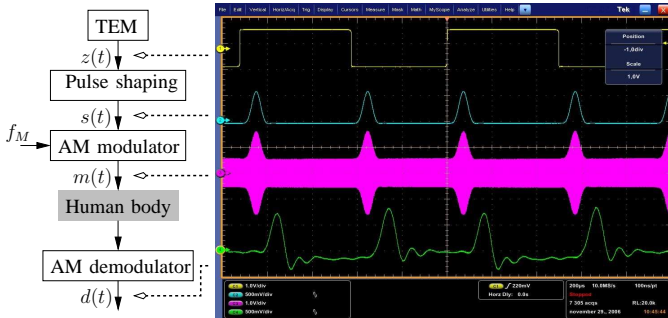

Fig. 8. Schematic of modulation and demodulation implemented with measured signals. The scope's sampling frequency is 10 MHz.

In our current HAN prototype the PDA recovers the T_k's from the demodulator output $d(t)$, digitizes them, and forwards the digitized T_k's for signal reconstruction at the remote site. As can be seen in the lowest trace of Fig. 8 the distance between the representative values of $d(t)$ above a certain level (such as the peaks) is about the same as the distance between the transitions of $z(t)$. This allows the extraction of

an approximation of the T_k's using a simple level-crossing scheme as shown in Fig. 9. From the output of a comparator
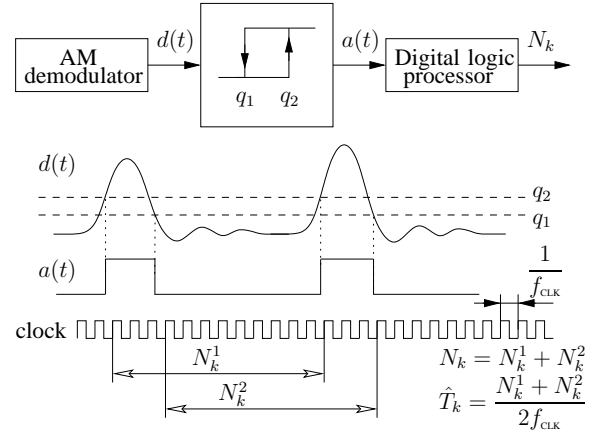

Fig. 9. Measurement of the T_k's based on the AM-demodulator output.

with hysteresis (Schmitt trigger) fed by $d(t)$ and a time-measuring clock, the digitized T_k's (denoted by $\hat{T}_k$ in the same figure) can be obtained by counting clock cycles and applying the simple formula shown. Note that the clock frequency f_{CLK} is known at the center (remote site). A software module carries out this algorithm using the samples of the demodulator output delivered by the digital oscilloscope. The hardware implementation using an 8 Mhz clock provided results that are in very good agreement with the ones of Figure 10. They are not included here because of space limitations.

IV. PERFORMANCE EVALUATION

In what follows we reconstruct the samples of a segment of $u(t)$ in Fig. 4(b) with and without noise or interference due to a neighboring channel. The same parameters for the input-signal bandwidth and the sampling frequency of the reconstructed signal are used as in Section III-B. The T_k's were determined by the algorithm implementing the functionality depicted in Fig. 9 with appropriate levels for q_1 and q_2. The evaluation is based on measuring the root-mean-square (RMS) error between the reconstructed samples $\hat{u}[kS]$ and the samples $u(kS)$ as described in Appendix VI-B.

A. Evaluation without Interference and Noise

In this section the reconstruction of the signal $u(t)$ is considered without sources of noise or interference. With levels $q_1 = 2.5$ and $q_2 = 2.7$, the T_k's were digitized by employing several time-measuring frequency values f_{CLK}. First, the number of bits needed to represent each N_k in Fig. 9 was determined. Then, the bit rate was calculated as the ratio of the total number of bits so obtained and the time interval over which the reconstruction was carried out. Fig. 10(a) shows the RMS reconstruction errors and the corresponding bit rate as a function of f_{CLK}. As seen, for high enough f_{CLK} values, the accuracy of the reconstruction is limited by circuit imperfections and the skin-surface channel. Fig. 10(b) shows the reconstructed samples with $f_{\text{CLK}} = 1$ GHz on a 1.9 s time range for $u(t)$.

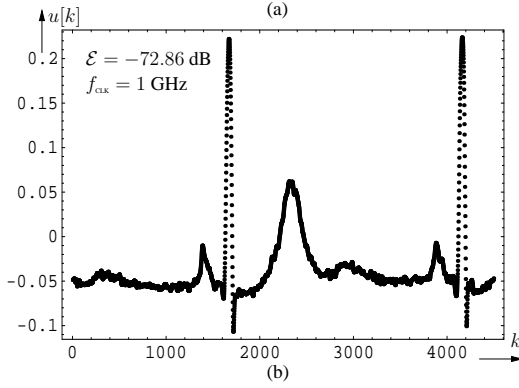| f_{clk} (Hz)	10^4	10^5	10^6	10^7	10^8
bitrate (kb/s)	8.65	17.3	23.8	30.3	38.9
$\mathcal{E}$ (dB)	-26.3	-30.3	-47.6	-66.8	-72.86

(a)

(b)

Fig. 10. Bitrate and RMS error for different f_{CLK} (a) (see Fig. 9), and reconstructed samples for a segment of $u(t)$ in Fig. 4(b) of length 1.9 s.

We note that these results were obtained by making tight contact with the skin. With loose contacts the signal level of the demodulator output drops and the reconstruction accuracy decreases.

B. Evaluation with Crosstalk from a Neighboring Sensor

In this experiment the auxiliary (dashed) signal generator in Fig. 3 was used to emulate the AM-modulator output
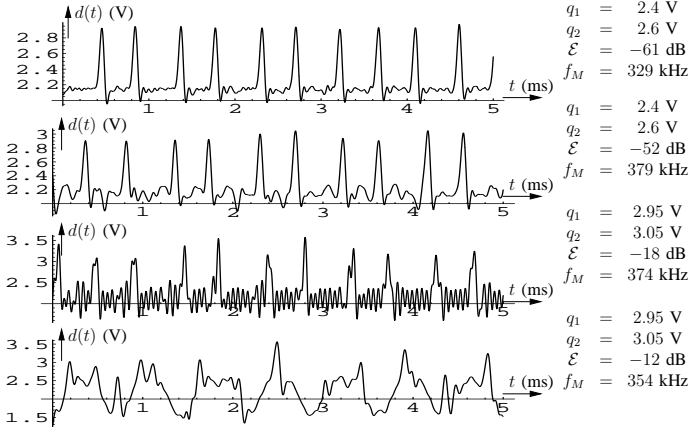

Fig. 11. Demodulator-output measurements with interfering AM-modulator at different carrier frequencies, f_M.

corresponding to the interfering sensor. In particular, a periodic $s(t)$ was created by the auxiliary signal generator with frequency of 2 kHz. This emulates the pulse-shaped signal corresponding to a TEM with zero input. Modulating this signal externally with a rectangular pulse stream with a frequency of 354 kHz models the interfering AM-modulator output. With several pulse-stream frequencies, f_M as carrier, the T_k's were determined and the reconstruction was carried out. In order to avoid errors due to the quantization of the T_k's, we used $f_{\text{CLK}} = 1$ GHz as in Fig. 10(b). Fig. 11 shows measured demodulator outputs including the values used for q_1, q_2, f_M, and the RMS reconstruction error $\mathcal{E}$. Comparing

the results with that of Fig. 10(b) a realistic, around 12 dB, performance degradation was experienced in the best case (top trace in Fig. 11).

C. Evaluation with Additive Noise

Finally, as in Fig. 3, a broadband noise generated by the auxiliary generator was added to the AM-modulator output. For the accurate level setting of signal and noise, the atten-

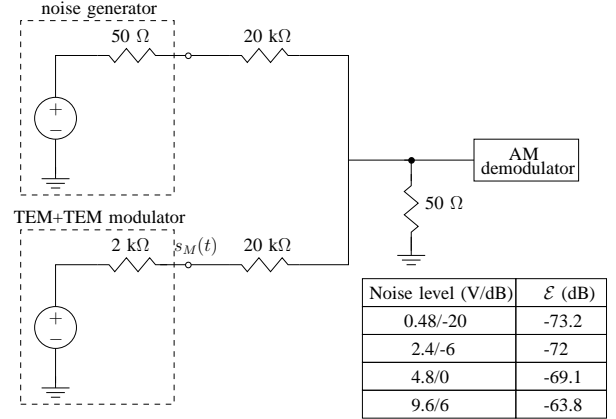| Noise level (V/dB)	$\mathcal{E}$ (dB)
0.48/-20	-73.2
2.4/-6	-72
4.8/0	-69.1
9.6/6	-63.8

Fig. 12. Circuit implementation for modeling additive noise and the attenuation due to the skin-surface channel and measured results.

uation of the skin-surface transmission was also emulated by the resistive voltage divider shown in Fig. 12.

As seen, the outputs of the AM-modulator and the noise source were taken into account by their Thévenin equivalents with Thévenin-resistances of 50 Ω and 2 kΩ, respectively. Using the resistances shown, a source of noise with RMS value 4.8 V turned out to give the same power at the demodulator input as that contributed by the AM-modulator output (noise level of 0 dB). For different noise levels reconstructions were carried out based on a time segment of 1.6 s with $f_{\text{CLK}} = 1$ GHz. Measured results are summarized in the table of Fig. 12. Although we have a narrowband receiver, the effect of a 6 dB noise is still visible in the demodulator output as shown in Fig. 13. The reconstructed signal samples with -63.8 dB reconstruction RMS error cannot be visually distinguished from the samples of $u(t)$. Thus, timing information is less sensitive than amplitude information to additive noise.

V. Conclusions

We have investigated an architecture for Human Area Networks that is based on representing biomonitoring information in the time domain and uses the skin surface to transmit this representation to a PDA. We demonstrated that the performance of such a system is above the biomonitoring requirements adopted in practice.

In our experimental environment we used a simple to implement AM modulation/demodulation scheme. Although AM-based schemes are sensitive to interference, the evaluation of our prototype has demonstrated a level of performance acceptable in biomonitoring applications. We expect to readily improve on our results by using better suited modulation schemes (e.g., FM).
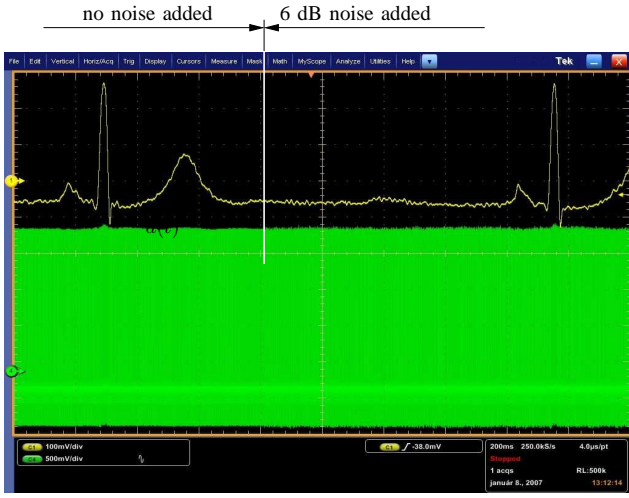
no noise added   6 dB noise added

Fig. 13. Measured results for the input (upper trace) and the effect of additive noise of 6 dB (lower trace). The scope's sampling frequency is 250 kHz.

Thus, the traditional HAN architecture consisting of clocked A/D converters feeding into digital RF channels can be replaced in biomonitoring applications with a less power demanding asynchronous TEM/TDM pair that uses the skin surface as a communications channel. We shall follow up on our work with the IC design of the main components of the HAN architecture.

VI. ACKNOWLEDGMENTS

APPENDIX

A. Parameter Insensitive Computation of the $\mathbf{d_i}$'s

Algorithm 2 The Vandermonde system in (9) can be reduced to an underdetermined linear system whose minimum-least-square and minimim-norm solution is given by

$$\mathbf{d}_i = b \left(\mathbf{x}_i - \frac{1}{\alpha_i} \mathbf{y}_i \mathbf{y}_i^H \mathbf{x}_i \right), \qquad \text{(A-1)}$$

where $\alpha_i = \mathbf{y}_i^H \mathbf{y}_i$ and, $\mathbf{x}_i$ and $\mathbf{y}_i$ denote the solutions of the Vandermonde systems

$$\mathbf{V}_i \mathbf{x}_i = \mathbf{D}_i (\mathbf{P} - \mathbf{a} \mathbf{b}^H) \mathbf{r}_i \qquad \text{(A-2)}$$

and

$$\mathbf{V}_i \mathbf{y}_i = \mathbf{D}_i \mathbf{a}, \qquad \text{(A-3)}$$

respectively, where $[\mathbf{r}_i]_n = (-1)^{i+n+1} T_{i+n}$ does not depend $\kappa\delta$, $\mathbf{a}^H = [\cdots, 0, 1, 0, 1]$, and $\mathbf{b}^H = [0, \cdots, 0, 0, 1]$.

B. Error Measures and Calibration

Our prototype TDM implementation in Mathematica [21] outputs the sequence (discrete-time signal) $\hat{u}[kS]$ that approximates the uniformly-spaced input samples $u(kS)$. The sampling period S and the signal bandwidth Ω are input parameters. The error sequence and its root-mean-square (RMS) value in dB defined as

$$\begin{aligned} e[k] &= u(kS) - \hat{u}[kS] \\ \text{and} \quad \mathcal{E} &= 10 \lg \left(\frac{\sum_{k=K_{\min}}^{K_{\max}} e^2[k]}{K_{\max} - K_{\min} + 1} \right), \end{aligned} \qquad \text{(A-4)}$$

respectively, quantify the quality of the TDM. Here $K_{\min}$ and $K_{\max}$ are appropriate integers.

Because of the periodicity of the generator output, absolute time in comparing the original and the reconstructed input cannot be used. Note that in order to use absolute time, some starting time t_0 and the corresponding value of $z(t)$ (δ or $-\delta$) is needed at the TDM site in addition to the T_k's. A constant delay between these has to be allowed. In addition, a DC offset and a constant scaling factor should also be included since (i) neither the circuit parameter b in (1) nor the generator tuning parameters are known with high accuracy and, (ii) TEM imperfections beyond the ideal TEM model of Fig. 2 (such as parameter offsets and frequency-dependent gain of opamps) also result in DC offset, constant scaling factor, and constant delay in the reconstructed signal [9]. Therefore, we again use the RMS error measure $\mathcal{E}$ of (A-4), but the error sequence is defined by

$$e[k] = \alpha u(kS - \tau) + \beta - \hat{u}[kS],$$

where the parameters α, β, and τ are chosen such that $\mathcal{E}$ is minimized. We developed a software algorithm for this optimization and used it in all performance evaluations.

We also sampled and measured the signal of Fig. 4(b) with the scope and, generated and evaluated u(kS) in the computational environment (see Fig. 3) with $S = 5$ μs. The RMS error between these two signals was -83 dB. This error as the ultimate precision limit for this setup is in agreement with the claimed 14-bit accuracy of both the scope and the generator.

REFERENCES

[1] M. Akay, *Time Frequency and Wavelets in Biomedical Signal Processing*, IEEE Press, Piscataway, 1998.

[2] E.V. Aksenov, Yu.M. Ljashenko, A.V. Plotnikov, D.A. Prilutskiy, S.V. Selishchev, E.V. Vetvetskiy, "Biomedical data acquisition systems based on sigma-delta analogue-to-digital converters" *in Proc. IEEE EMBS 23rd Annual International Conference*, Oct. 2001, vol. 4, pp. 3336-3337.

[3] E. Allier, J. Goulier, G. Sicard, A. Dezzani, E. Andre, M. Renaudin, "A 120nm Low Power Asynchronous ADC", *Proceedings of the 2005 International Symposium on Low Power Electronics and Design*, San Diego, CA, 2005, pp. 60-65.

[4] H.G. Feichtinger, K. Gróchenig and T. Strohmer, "Efficient Numerical Methods in Non-uniform Sampling Theory", *Numerische Mathematik*, Vol. 69, pp. 423-440, 1995.

[5] G.H. Golub, C.F. Van Loan, *Matrix Computations*, Third edition, The John Hopkins University Press, 1996.

[6] E. Jovanov, A. Milenkovic, C. Otto, and P.C. de Groen, "A wireless body area network of intelligent motion sensors for computer assisted physical rehabilitation", *Journal of NeuroEngineering and Rehabilitation*, March 2005, pp. 1-10.

[7] B. Kenneth and K. Asanovic, "Energy aware lossless data compression", *Proceedings of the 1st international conference on Mobile systems, applications and services*, pp. 231-244, 2003, San Francisco CA, USA.

[8] C.J. Kikkert, and D.J. Miller, "Asynchronous delta sigma modulation", *Proceedings of the IREE (Australia)*, Vol. 36, pp. 83-88, April 1975.

[9] P.R. Kinget, A.A. Lazar and L.T. Toth, "On the Robustness of the VLSI Implementation of a Time Encoding Machine", *Proceedings of ISCAS 2005*, May 23-26, 2005, Kobe.

[10] N. Krishnapura, S. Pavan, C. Mathiazhagan, B. Ramamurthi, "A baseband pulse shaping filter for Gaussian minimum shift keying", *The 1998 IEEE International Symposium on Circuits and Systems, ISCAS'98* , vol. 1, pp. 249-252, May 31 - June 3, 1998, Monterey, CA, USA.

[11] A.A. Lazar and L.T. Tóth, "Perfect Recovery and Sensitivity Analysis of Time Encoded Bandlimited Signals", *IEEE Transactions on Circuits and Systems-I: Regular Papers*, Vol. 51, No 10, pp. 2060-2073, October 2004.

[12] A.A. Lazar, "Time Encoding with an Integrate-and fire Neuron with a Refractory Period", *Neurocomputing*, Vol. 58-60, pp. 53- 58, 2004.

[13] A.A. Lazar, E.K. Simonyi, and L.T. Tóth, "An overcomplete stitching algorithm for time decoding machines", submitted for publication.

[14] A.A. Lazar, "Time Encoding Machines with Multiplicative Coupling, Feedforward and Feedback", *IEEE Transactions on Circuits and Systems-II: Express Briefs*, Vol. 53, No. 8, pp. 672-676, August 2006.

[15] MIT-BIH Arrhythmia Database, http://www.physionet.org/physiobank/database/mitdb/

[16] S. Ouzounov, E. Roza, J. A. Hegt, G. van der Weide and A.H.M. van Roermund, "Analysis and Design of High-Performance Asynchronous Sigma-Delta Modulators with a Binary Quantizer", *IEEE Journal of Solid-State Circuits*, Vol. 41, No. 3, March 2006, pp. 588-596.

[17] E. Roza, "Analog-to-digital conversion via duty-cycle modulation", *IEEE Transactions on Circuits and Systems-II: Analog and Digital Signal Processing*, Vol. 44, No. 11, pp. 907-917, November 1997.

[18] H.Y. Yang and R. Sarpeshkar, "A Bio-inspired ultra-energy-efficient analog-to-digital Converter for biomedical applications", *IEEE Transactions on Circuits and Systems, Regular Papers* , vol. 53, no. 11, November 2006, pp. 2349-2356.

[19] M. Shinagawa, M. Fukumoto, K. Ochiai, and H. Kyuragi, "A Near-Field-Sensing Transceiver for Intrabody Communication Based on the Electrooptic Effect", *IEEE Transactions on Instrumentation and Measurement*, Vol. 53, No. 6, December 2004, pp. 1533-1538.

[20] D. Wei and J.G. Harris, "Signal Reconstruction from Spiking Neuron Models", *Proceedings of the ISCAS'04*, Vol. V, pp. 353- 356, May 23-26, 2004, Vancouver, Canada.

[21] S. Wolfram, *The Mathematica Book Online*, http://documents.wolfram.com/mathematica/

[22] T.G. Zimmerman, *Personal Area Networks (PAN): Near-Field Intra-Body Communicatio*, MS Thesis, MIT, September 1995.

[23] T. G. Zimmerman, "Personal Area Networks: Near-field intrabody communication", IBM SYSTEMS JOURNAL, VOL 35, 1996, pp. 611-617.